Perfectly Matched Layer Mesh Terminations for Nodal-Based Finite-Element Methods in Electromagnetic Scattering

Jingwu Tang, Keith D. Paulsen, and Shah A. Haider

***Abstract*— The perfectly matched layer (PML) concept introduced by Berenger is implemented for nodal-based finite-element frequency-domain methods. Starting from a scalar/vector potential framework, anisotropic-media-equivalent gauge conditions are developed for both coupled and uncoupled (i.e., direct field) scalar/vector field formulations. The resulting discrete system of equations are shown to be identical for both the anisotropic and stretched coordinate viewpoints of PML mesh termination on node-based finite elements. Reaching this equivalency requires that special attention be paid to the basis/weighting functions used within the PML region, specifically, a material dependency is found to be essential. The alternative but identical stretched coordinate approach provides the perspective needed to realize a scheme for generalizing the PML to non-Cartesian mesh terminations which are more natural in the finite-element context. Several benchmark problems and associated numerical results are presented to demonstrate the performance of the PML on node-based finite elements.**

***Index Terms*—Electromagnetic scattering, finite-element methods, perfectly matched layer.**

I. Introduction

THERE has been considerable interest in the development, implementation, and interpretation of the perfectly matched layer (PML) concept, first introduced by Beringer [1] as an effective mesh-truncation scheme for differential equation solutions in computational electromagnetics (e.g., [2]–[10]). Investigation has spawned two views of the PML approach: 1) a coordinate stretching construct involving a complex-valued coordinate transformation, which alters the spatial derivative operators in Maxwell's equations [3], [4] and 2) an anisotropic material formulation where the Maxwell equations retain their familiar forms, but with the insertion of complex material property tensors for the permittivity and permeability within the layer [2]. More recent analysis has shown the mathematical equivalence of these two approaches [6], [9], although close scrutiny reveals that the continuity conditions on the normal field components will, in general, be different leading to different normal fields between the two schemes [6].

Manuscript received April 14, 1997; revised December 8, 1997. This work was supported by National Institutes of Health Grant RO1-CA37245, awarded by the National Cancer Institute.

The authors are with the Thayer School of Engineering, Dartmouth College, Hanover, NH 03755 USA.

Publisher Item Identifier S 0018-926X(98)02677-5.

On the implementation/validation front, the majority of attention to date has been devoted to finite-difference time-domain (FDTD) considerations [3], [5], [8], [9] although there has been a significant increase in the development and use of the PML in finite-element (FE) frequency-domain scattering calculations as well [2], [6]. In this regard, edge-element formulations have served as the primary focus and have dominated the advances that have been reported in the literature for finite elements. In both the FDTD and FE cases, the results reported appear to be largely positive. Parameters of interest (e.g., layer thickness, material properties, and distance from the scatterers) have been studied and a certain amount of fine-tuning and selection guidelines for setting these parameters has developed. Some iterative solution convergence difficulties have been noted [6], which have constrained property value choices; nonetheless, the success of the PML to date along with its relative ease of implementation, compared to alternatives, suggests that it may become the method of choice for mesh truncation with differential equation approaches to electromagnetic (EM) scattering problems.

In this paper, we report on the development of PML analogs for node-based finite-element discretizations. We show that the PML concept can be efficiently and effectively incorporated into the node-based scalar/vector potential framework of Boyse *et al.* [11], which is free of spurious solutions at least in the absence of perfectly conducting sharp corners, although some progress on this front has been recently realized [12]. Specifically, we demonstrate that the PML can be implemented in both Lorentz gauge #2 and Lorentz gauge #1 from [11], the former leading to a coupled set of continuous scalar/vector potential equations [13], while the later produces an uncoupled pair, which, under proper boundary condition specification, results in a direct field formulation [11], [14]. An interesting and important feature of our numerical approach is the fact that both the anisotropic media and stretched coordinate viewpoints of mesh truncation in this context lead to the same discrete system of equations and hence are numerically identical. This is accomplished through the careful selection of material dependent basis/weighting functions that satisfy all jump conditions while also preserving matrix symmetry. Further, these parallel views are used to identify an implementation strategy for realizing the PML on node-based finite elements, which is generalized to non-Cartesian mesh terminations that not only preserves the flexibility of the finite-element method (FEM) in terms of accommodating complex geometries, but also relieves

the imposition of any constraints on the already difficult task of three-dimensional (3-D) mesh generation when the PML is employed.

In the following sections, we develop the node-based PML construct in terms of the scalar/vector potential framework by deriving the associated gauge conditions and weak forms. The importance of selecting material dependent basis functions within the layer is illustrated. Results from several sample benchmark problems, including examples with non-Cartesian mesh terminations are highlighted to demonstrate the validity and overall performance of the PML within the node-based finite element computational framework.

II. Anisotropic Scalar/Vector Potential Weak Forms

Following the notation of Zhao and Cangellaris [9], we begin with the Maxwell equations in anisotropic source-free media

$$\nabla \times \vec{E} = i\omega \overline{\mu} \cdot \vec{H} \tag{1}$$

$$\nabla \times \vec{H} = -i\omega \overline{\epsilon} \cdot \vec{E} \tag{2}$$

$$\nabla \cdot \overline{\epsilon} \cdot \vec{E} = 0 \tag{3}$$

$$\nabla \cdot \overline{\mu} \cdot \vec{H} = 0 \tag{4}$$

where $\overline{\mu}$ and $\overline{\epsilon}$ are the permeability and permittivity tensors which have diagonal forms [2], [9]

$$\overline{\epsilon} = \epsilon \Lambda \tag{5}$$

$$\overline{\mu} = \mu \Lambda \tag{6}$$

such that

$$[\Lambda] = \operatorname{diag}\{a_1, a_2, a_3\}. \tag{7}$$

As shown in [2] and elsewhere, a_1, a_2, and a_3 are complex constants that take on a special relationship in the absorbing layer in order to preserve its perfect match with the interior domain. Introducing the vector and scalar potentials $\vec{A}$ and Φ defined as

$$\overline{\mu} \cdot \vec{H} = \nabla \times \vec{A} \tag{8}$$

$$\vec{E} = i\omega \vec{A} - \nabla \Phi \tag{9}$$

into (2) and (3) yields the coupled equations [whose solution also satisfies (1) and (4) provided the appropriate gauge and boundary conditions are satisfied]

$$\nabla \times \frac{1}{\mu} \Lambda^{-1} \cdot \nabla \times \vec{A} - \omega^2 \overline{\epsilon} \cdot \vec{A} - i\omega \overline{\epsilon} \cdot \nabla \Phi = 0 \tag{10}$$

$$\nabla \cdot \overline{\epsilon} \cdot (i\omega \vec{A} - \nabla \Phi) = 0 \tag{11}$$

which are identical to those in [11] with ϵ and μ replaced by their tensor counterparts $\overline{\epsilon}$ and $\overline{\mu}$.

Motivated by the generality of the approach in [9], we can identify a set of scaled potentials, which are simply related to the true potentials as

$$\vec{A} = G \cdot \hat{A} \tag{12}$$

$$\Phi = \hat{\Phi} \tag{13}$$

where G is a constant diagonal scaling matrix

$$[G] = \operatorname{diag}\{g_1, g_2, g_3\}. \tag{14}$$

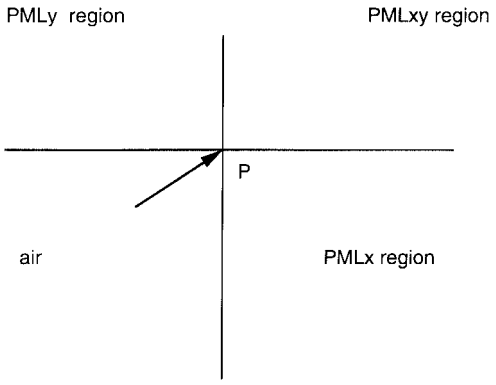

Fig. 1. Point P connecting to multiple materials.

$\vec{A} = \{A_x, A_y, A_z\}^T$ and Φ are the true potentials and $\hat{A} = \{\hat{A}_x, \hat{A}_y, \hat{A}_z\}^T$ and $\hat{\Phi}$ are their scaled versions provided that the scaling factors g_1, g_2, g_3 are chosen such that

$$\left(\frac{g_1}{g_2}\right)^2 = \frac{a_2}{a_1}, \left(\frac{g_2}{g_3}\right)^2 = \frac{a_3}{a_2}, \left(\frac{g_3}{g_1}\right)^2 = \frac{a_1}{a_3}. \tag{15}$$

This mapping when introduced into (10) and (11) produces the coupled system of equations for the scaled potentials in isotropic media

$$\nabla_a \times \frac{1}{\mu} \nabla_a \times \hat{A} - \omega^2 \epsilon \hat{A} - i\omega \epsilon \nabla_a \hat{\Phi} = 0 \tag{16}$$

$$\nabla_a \cdot \epsilon (i\omega \hat{A} - \nabla_a \hat{\Phi}) = 0 \tag{17}$$

where

$$\nabla_a \stackrel{\text{def}}{=} \hat{x} \frac{1}{g_1} \partial_x + \hat{y} \frac{1}{g_2} \partial_y + \hat{z} \frac{1}{g_3} \partial_z. \tag{18}$$

Equations (16) and (17) are readily recognized as the vector/scalar potential representations of the isotropic Maxwell forms

$$\nabla_a \times \hat{E} = i\omega \mu \hat{H} \tag{19}$$

$$\nabla_a \times \hat{H} = -i\omega \epsilon \hat{E} \tag{20}$$

$$\nabla_a \cdot \epsilon \hat{E} = 0 \tag{21}$$

$$\nabla_a \cdot \mu \hat{H} = 0 \tag{22}$$

which means that we can follow the development in [11] in order to identify two possible gauge conditions

$$\nabla_a \cdot \epsilon \hat{A} = i\omega \epsilon^2 \mu^{\Phi} \tag{23}$$

$$\nabla_a \cdot \hat{A} = i\omega \epsilon \mu \hat{\Phi} \tag{24}$$

corresponding to Lorentz gauge #1 and Lorentz gauge #2, respectively. Transforming these relationships back in terms of the true potentials in anisotropic medium leads to

$$\nabla \cdot \epsilon \Lambda \cdot \vec{A} = a_1 a_2 a_3 i\omega \epsilon^2 \mu \Phi \tag{25}$$

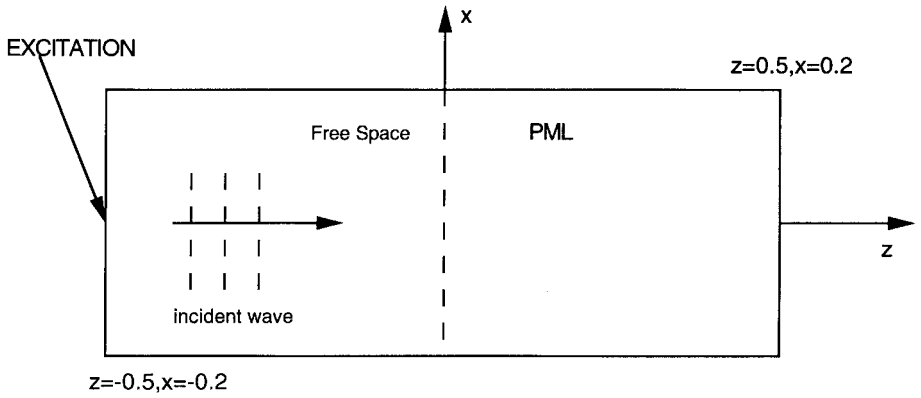

Fig. 2. Geometry of the computational domain for benchmark problem 1—a plane wave normally incident on a PML.

$$\nabla \cdot \Lambda \cdot \vec{A} = a_1 a_2 a_3 i\omega\epsilon\mu\Phi \tag{26}$$

which become the desired gauge conditions for implementing the PML within the scalar/vector potential framework.

Realizing a node-based discrete system under Lorentz gauge #2 begins by substituting (26) into (10) and (11), which yields

$$\nabla \times \frac{1}{\mu}\Lambda^{-1} \cdot \nabla \times \vec{A} - \omega^2\epsilon\Lambda \cdot \vec{A} - \Lambda \cdot \nabla \frac{1}{\mu a_1 a_2 a_3}\nabla \cdot (\Lambda \cdot \vec{A}) + i\omega\Phi\Lambda \cdot \nabla\epsilon = 0 \tag{27}$$

$$-\nabla \cdot \epsilon\Lambda \cdot \nabla\Phi + \Lambda \cdot i\omega\vec{A} \cdot \nabla\epsilon - \omega^2\epsilon^2\mu a_1 a_2 a_3 \Phi = 0. \tag{28}$$

Weighted residual treatment of (27) and (28) follows analogously from that presented in Paulsen *et al.* [13], which, in this case, results in the weak forms

$$\begin{aligned}
&\left\langle \nabla\phi_i \times \frac{1}{\mu}\Lambda^{-1} \cdot \nabla \times \vec{A} \right\rangle + \left\langle \frac{1}{\mu a_1 a_2 a_3}\nabla \cdot (\Lambda \cdot \vec{A})\,(\Lambda \cdot \nabla\phi_i) \right\rangle \\
&\quad - \langle i\omega\epsilon(\Lambda \cdot \nabla)\,(\Phi\phi_i)\rangle - \langle \omega^2\epsilon\Lambda \cdot \vec{A}\phi_i \rangle \\
&\quad = -\oint \hat{n} \times \left(\frac{1}{\mu}\Lambda^{-1} \cdot \nabla \times \vec{A}\right)\phi_i d_S + \oint (\Lambda \cdot \hat{n}) \\
&\quad \cdot \left[\frac{1}{\mu a_1 a_2 a_3}\nabla \cdot (\Lambda \cdot \vec{A}) - i\omega\Phi\epsilon\right]\phi_i d_S
\end{aligned} \tag{29}$$

$$A_{ij} = \begin{bmatrix}
\left\langle \frac{1}{\mu}\left(\frac{a_1}{a_2 a_3}\frac{\partial\phi_j}{\partial x}\frac{\partial\phi_i}{\partial x} + \frac{1}{a_3}\frac{\partial\phi_j}{\partial y}\frac{\partial\phi_i}{\partial y} + \frac{1}{a_2}\frac{\partial\phi_j}{\partial z}\frac{\partial\phi_i}{\partial z}\right) - \omega^2\epsilon a_1\phi_i\phi_j \right\rangle & \left\langle \frac{1}{\mu a_3}\left(-\frac{\partial\phi_j}{\partial x}\frac{\partial\phi_i}{\partial y} + \frac{\partial\phi_j}{\partial y}\frac{\partial\phi_i}{\partial x}\right)\right\rangle \\
\left\langle \frac{1}{\mu a_3}\left(-\frac{\partial\phi_j}{\partial y}\frac{\partial\phi_i}{\partial x} + \frac{\partial\phi_j}{\partial x}\frac{\partial\phi_i}{\partial y}\right)\right\rangle & \left\langle \frac{1}{\mu}\left(\frac{1}{a_3}\frac{\partial\phi_j}{\partial x}\frac{\partial\phi_i}{\partial x} + \frac{a_2}{a_3 a_1}\frac{\partial\phi_j}{\partial y}\frac{\partial\phi_i}{\partial y} + \frac{1}{a_1}\frac{\partial\phi_j}{\partial z}\frac{\partial\phi_i}{\partial z}\right) - \omega^2\epsilon a_2\phi_i\phi_j \right\rangle \\
\left\langle \frac{1}{\mu a_2}\left(-\frac{\partial\phi_j}{\partial z}\frac{\partial\phi_i}{\partial x} + \frac{\partial\phi_j}{\partial x}\frac{\partial\phi_i}{\partial z}\right)\right\rangle & \left\langle \frac{1}{\mu a_1}\left(-\frac{\partial\phi_j}{\partial z}\frac{\partial\phi_i}{\partial y} + \frac{\partial\phi_j}{\partial y}\frac{\partial\phi_i}{\partial z}\right)\right\rangle \\
\left\langle -i\omega\epsilon a_1\left(\phi_j\frac{\partial\phi_i}{\partial x} + \phi_i\frac{\partial\phi_j}{\partial x}\right)\right\rangle & \left\langle -i\omega\epsilon a_2\left(\phi_j\frac{\partial\phi_i}{\partial y} + \phi_i\frac{\partial\phi_j}{\partial y}\right)\right\rangle
\end{bmatrix}$$

$$\begin{bmatrix}
\left\langle \frac{1}{\mu a_2}\left(-\frac{\partial\phi_j}{\partial x}\frac{\partial\phi_i}{\partial z} + \frac{\partial\phi_j}{\partial z}\frac{\partial\phi_i}{\partial x}\right)\right\rangle & \left\langle -i\omega\epsilon a_1\left(\phi_j\frac{\partial\phi_i}{\partial x} + \phi_i\frac{\partial\phi_j}{\partial x}\right)\right\rangle \\
\left\langle \frac{1}{\mu a_1}\left(-\frac{\partial\phi_j}{\partial y}\frac{\partial\phi_i}{\partial z} + \frac{\partial\phi_j}{\partial z}\frac{\partial\phi_i}{\partial y}\right)\right\rangle & \left\langle -i\omega\epsilon a_2\left(\phi_j\frac{\partial\phi_i}{\partial y} + \phi_i\frac{\partial\phi_j}{\partial y}\right)\right\rangle \\
\left\langle \frac{1}{\mu}\left(\frac{1}{a_2}\frac{\partial\phi_j}{\partial x}\frac{\partial\phi_i}{\partial x} + \frac{1}{a_1}\frac{\partial\phi_j}{\partial y}\frac{\partial\phi_i}{\partial y} + \frac{a_3}{a_1 a_2}\frac{\partial\phi_j}{\partial z}\frac{\partial\phi_i}{\partial z}\right) - \omega^2\epsilon a_3\phi_i\phi_j \right\rangle & \left\langle -i\omega\epsilon a_3\left(\phi_j\frac{\partial\phi_i}{\partial z} + \phi_i\frac{\partial\phi_j}{\partial z}\right)\right\rangle \\
\left\langle -i\omega\epsilon a_3\left(\phi_j\frac{\partial\phi_i}{\partial z} + \phi_i\frac{\partial\phi_j}{\partial z}\right)\right\rangle & \left\langle \epsilon\left(a_1\frac{\partial\phi_i}{\partial x}\frac{\partial\phi_j}{\partial x} + a_2\frac{\partial\phi_i}{\partial y}\frac{\partial\phi_j}{\partial y} + a_3\frac{\partial\phi_i}{\partial z}\frac{\partial\phi_j}{\partial z}\right) - \omega^2\epsilon^2\mu a_1 a_2 a_3\phi_i\phi_j \right\rangle
\end{bmatrix} \tag{30b}$$

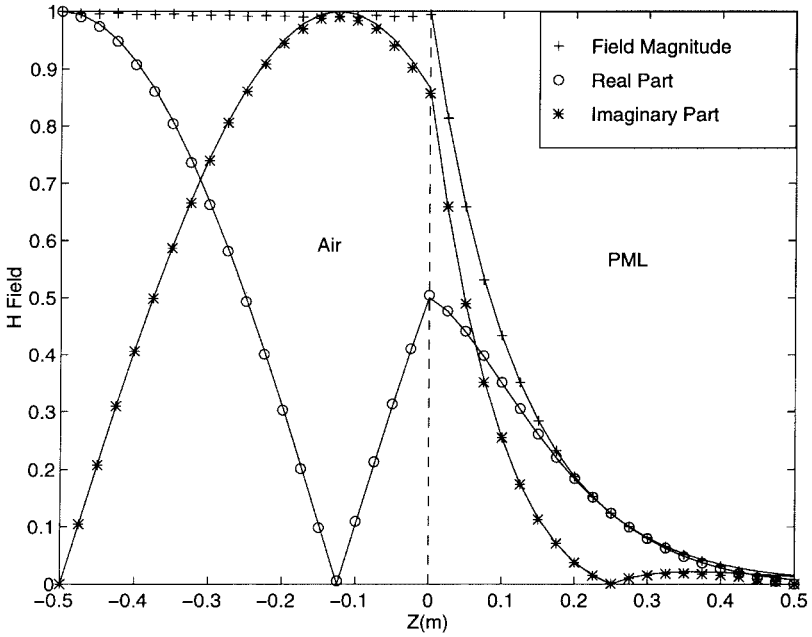

Fig. 3. Comparsion of the numerical (markers) and analytical (solidline) solution for benchmark problem 1.

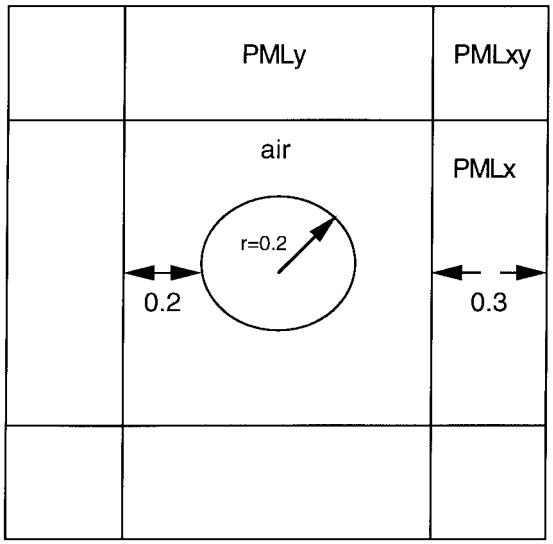

Fig. 4. Schematic of the geometry of benchmark problem 2—the cylindrical radiator.

$$\langle -\nabla\phi_i \cdot \epsilon\Lambda \cdot \nabla\Phi\rangle + \langle \omega^2\epsilon^2\mu a_1 a_2 a_3 \Phi\phi_i\rangle + \langle i\omega\epsilon\nabla\cdot(\phi_i\Lambda\cdot\vec{A})\rangle = \oint \hat{n}\cdot\epsilon(i\omega\Lambda\cdot\vec{A} - \Lambda\cdot\nabla\Phi)\phi_i d_S \tag{30a}$$

where $\langle\cdot\rangle$ represents domain integration and $\oint$ denotes integration over the enclosing boundary. Spatial expansion of $\vec{A}$ and Φ in the nodal basis functions ϕ_i leads to a single symmetric algebraic system $A_{ij}F_j = R_j$ where as shown in (30b) at the bottom of the previous page.

Similarly, using anisotropic Lorentz gauge #1, i.e., (25), we can obtain the corresponding $\vec{H}$ and $\vec{E}$ formulations for anisotropic medium

$$\nabla\times\frac{1}{i\omega\epsilon}\Lambda^{-1}\cdot\nabla\times\vec{H} - \Lambda\cdot\nabla\left(\frac{1}{i\omega\epsilon a_1 a_2 a_3}\nabla\cdot\Lambda\cdot\vec{H}\right) + i\omega\mu\Lambda\cdot\vec{H} = 0 \tag{31}$$

$$\nabla\times\frac{1}{i\omega\mu}\Lambda^{-1}\cdot\nabla\times\vec{E} - \epsilon\Lambda\cdot\nabla\left(\frac{1}{i\omega\mu\epsilon^2 a_1 a_2 a_3}\nabla\cdot\epsilon\Lambda\cdot\vec{E}\right) + i\omega\epsilon\Lambda\cdot\vec{E} = 0. \tag{32}$$

With either of the two derived gauged conditions, the finite-element matrix A_{ij} not only remains symmetric, but also preserves many of the desirable properties of the corresponding matrices for isotropic media [13]. For example, if either node i or node j is not on a boundary or material interface, the off-diagonal terms in A_{ij} will be zero which significantly reduces the number of nonzero entries within the completely assembled sparse matrix system.

III. Material Dependent Bases

To employ the PML technique in 3-D calculations, we need six PML faces, 12 PML edges, and eight PML corners as described by Zhao and Cangellaris [9] to enclose the rectangular volume in which electromagnetic interactions are calculated. In order to make these PML regions reflectionless, matrix Λ takes on a special form in each case. For example, following the notation in [9], the matrix Λ will be

$$\Lambda^{(z)} = \mathrm{diag}\left\{a_z,\ a_z,\ \frac{1}{a_z}\right\} \tag{33}$$

$$\Lambda^{(zx)} = \mathrm{diag}\left\{\frac{a_z}{a_x},\ a_z a_x,\ \frac{a_x}{a_z}\right\} \tag{34}$$

$$\Lambda^{(xyz)} = \mathrm{diag}\left\{\frac{a_y a_z}{a_x},\ \frac{a_z a_x}{a_y},\ \frac{a_x a_y}{a_z}\right\} \tag{35}$$

in the PMLz, PMLzx, PMLxyz regions, respectively. Here, PMLz corresponds to the PML region containing the face of the rectangular volume whose normal is in the z direction. PMLzx is the PML region corresponding to the volume

containing the common edge which separates the PMLx and PMLz faces. PMLxyz is the PML region corresponding to the corner cuboid which separates the PMLzx, PMLxy, and PMLyz edges.

In isotropic media, $\vec{A}$ is continuous across all material interfaces when Lorentz gauge #2 is used. However, this is no longer the case when the Lorentz gauge #2 equivalent for anisotropic media [i.e., (26)] is employed. Specifically, $\vec{A}$ is discontinous across different PML materials and at the PML interface with the interior (isotropic) domain. For example, at a planar interface between air (i.e., the interior) and the PMLx region, the boundary conditions require a jump in the x component of $\vec{A}$ (normal to the plane) and continuity in the y and z components of $\vec{A}$ (tangential to the plane)

$$\frac{1}{a_x}A_x^{\mathrm{PML}x} = A_x^{\mathrm{air}} \tag{36}$$

$$A_y^{\mathrm{PML}x} = A_y^{\mathrm{air}} \tag{37}$$

$$A_z^{\mathrm{PML}x} = A_z^{\mathrm{air}}. \tag{38}$$

This causes some difficulty for nodal FEM's using conventional basis functions because of the multiplicity of solution values at nodes, which connect multiple materials. For example, at point P in Fig. 1, vector potential $\vec{A}$ will have four different values in the four different regions and they need to satisfy the following relationships:

$$\vec{A}_x^{air} = \vec{A}_x^{\mathrm{PML}y} = \frac{1}{a_x}\vec{A}_x^{\mathrm{PML}x} = \frac{1}{a_x}\vec{A}_x^{\mathrm{PMLxy}} \tag{39}$$

$$\vec{A}_y^{air} = \vec{A}_y^{\mathrm{PML}x} = \frac{1}{a_y}\vec{A}_y^{\mathrm{PML}y} = \frac{1}{a_y}\vec{A}_x^{\mathrm{PMLxy}} \tag{40}$$

$$\vec{A}_z^{air} = \vec{A}_z^{\mathrm{PML}y} = \vec{A}_z^{\mathrm{PML}x} = \vec{A}_z^{\mathrm{PMLxy}}. \tag{41}$$

However, we find that if we use material dependent basis functions we can overcome this problem. Specifically, the basis functions become

$$\begin{aligned}
\text{interior domain}: &\quad (\phi_i,\ \phi_i,\ \phi_i)\\
\mathrm{PML}x: &\quad (a_x\phi_i,\ \phi_i,\ \phi_i)\\
\mathrm{PML}y: &\quad (\phi_i,\ a_y\phi_i,\ \phi_i)\\
\mathrm{PML}z: &\quad (\phi_i,\ \phi_i,\ a_z\phi_i)\\
\mathrm{PML}xy: &\quad (a_x\phi_i,\ a_y\phi_i,\ \phi_i)\\
\mathrm{PML}yz: &\quad (\phi_i,\ a_y\phi_i,\ a_{z\,\phi i})\\
\mathrm{PML}zx: &\quad (a_x\phi_i,\ \phi_i,\ a_{z\,\phi i})\\
\mathrm{PML}xyz: &\quad (a_x\phi_i,\ a_{y\,\phi i},\ a_{z\,\phi i})
\end{aligned} \tag{42}$$

where ϕ_i is the conventional linear basis function at node i, which has value one at node i and zero at other nodes. Notation

$$\begin{bmatrix}
\left\langle \frac{1}{\mu}\left(\frac{1}{a}\frac{\partial\phi_j}{\partial x}\frac{\partial\phi_i}{\partial x} + a\frac{\partial\phi_j}{\partial y}\frac{\partial\phi_i}{\partial y} + a\frac{\partial\phi_j}{\partial z}\frac{\partial\phi_i}{\partial z}\right) - \omega^2\epsilon a\phi_i\phi_j \right\rangle & \left\langle \frac{1}{\mu}\left(-\frac{\partial\phi_j}{\partial x}\frac{\partial\phi_i}{\partial y} + \frac{\partial\phi_j}{\partial y}\frac{\partial\phi_i}{\partial x}\right)\right\rangle \\
\left\langle \frac{1}{\mu}\left(-\frac{\partial\phi_j}{\partial y}\frac{\partial\phi_i}{\partial x} + \frac{\partial\phi_j}{\partial x}\frac{\partial\phi_i}{\partial y}\right)\right\rangle & \left\langle \frac{1}{\mu}\left(\frac{1}{a}\frac{\partial\phi_j}{\partial x}\frac{\partial\phi_i}{\partial x} + a\frac{\partial\phi_j}{\partial y}\frac{\partial\phi_i}{\partial y} + a\frac{\partial\phi_j}{\partial z}\frac{\partial\phi_i}{\partial z}\right) - \omega^2\epsilon a\phi_i\phi_j \right\rangle \\
\left\langle \frac{1}{\mu}\left(-\frac{\partial\phi_j}{\partial z}\frac{\partial\phi_i}{\partial x} + \frac{\partial\phi_j}{\partial x}\frac{\partial\phi_i}{\partial z}\right)\right\rangle & \left\langle \frac{a}{\mu}\left(-\frac{\partial\phi_j}{\partial z}\frac{\partial\phi_i}{\partial y} + \frac{\partial\phi_j}{\partial y}\frac{\partial\phi_i}{\partial z}\right)\right\rangle \\
\left\langle -i\omega\epsilon\left(\phi_j\frac{\partial\phi_i}{\partial x} + \phi_i\frac{\partial\phi_j}{\partial x}\right)\right\rangle & \left\langle -i\omega\epsilon a\left(\phi_j\frac{\partial\phi_i}{\partial y} + \phi_i\frac{\partial\phi_j}{\partial y}\right)\right\rangle
\end{bmatrix}$$

$$\begin{bmatrix}
\left\langle \frac{1}{\mu}\left(-\frac{\partial\phi_j}{\partial x}\frac{\partial\phi_i}{\partial z} + \frac{\partial\phi_j}{\partial z}\frac{\partial\phi_i}{\partial x}\right)\right\rangle & \left\langle -i\omega\epsilon\left(\phi_j\frac{\partial\phi_i}{\partial x} + \phi_i\frac{\partial\phi_j}{\partial x}\right)\right\rangle \\
\left\langle \frac{a}{\mu}\left(-\frac{\partial\phi_j}{\partial y}\frac{\partial\phi_i}{\partial z} + \frac{\partial\phi_j}{\partial z}\frac{\partial\phi_i}{\partial y}\right)\right\rangle & \left\langle -i\omega\epsilon a\left(\phi_j\frac{\partial\phi_i}{\partial y} + \phi_i\frac{\partial\phi_j}{\partial y}\right)\right\rangle \\
\left\langle \frac{1}{\mu}\left(\frac{1}{a}\frac{\partial\phi_j}{\partial x}\frac{\partial\phi_i}{\partial x} + a\frac{\partial\phi_j}{\partial y}\frac{\partial\phi_i}{\partial y} + a\frac{\partial\phi_j}{\partial z}\frac{\partial\phi_i}{\partial z}\right) - \omega^2\epsilon a\phi_i\phi_j \right\rangle & \left\langle -i\omega\epsilon a\left(\phi_j\frac{\partial\phi_i}{\partial z} + \phi_i\frac{\partial\phi_j}{\partial z}\right)\right\rangle \\
\left\langle -i\omega\epsilon a\left(\phi_j\frac{\partial\phi_i}{\partial z} + \phi_i\frac{\partial\phi_j}{\partial z}\right)\right\rangle & \left\langle \epsilon\left(\frac{1}{a}\frac{\partial\phi_i}{\partial x}\frac{\partial\phi_j}{\partial x} + a\frac{\partial\phi_i}{\partial y}\frac{\partial\phi_j}{\partial y} + a\frac{\partial\phi_i}{\partial z}\frac{\partial\phi_j}{\partial z}\right) - \omega^2\epsilon^2\mu a\phi_i\phi_j \right\rangle
\end{bmatrix} \tag{43b}$$

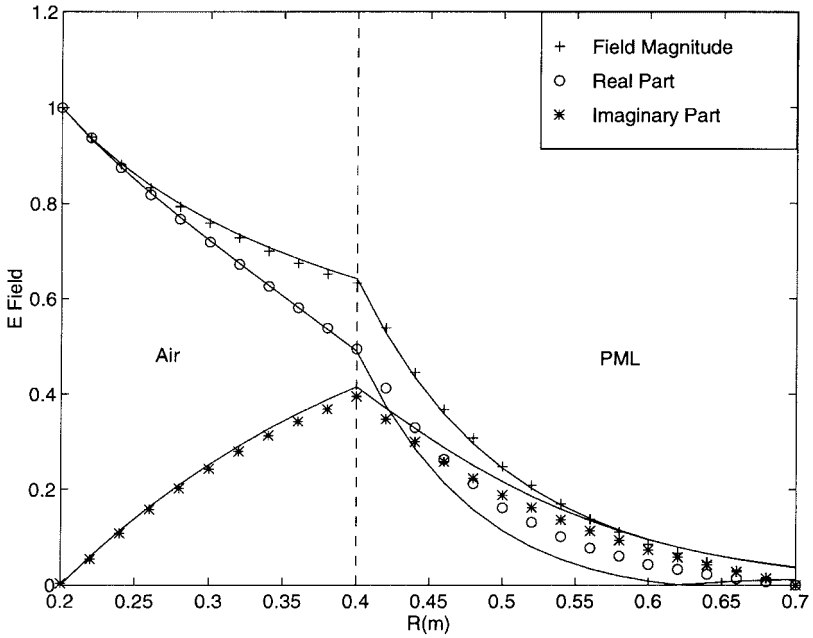

Fig. 5. Comparsion of the numerical (markers) and analytical (solid line) solution for benchmark problem 2.

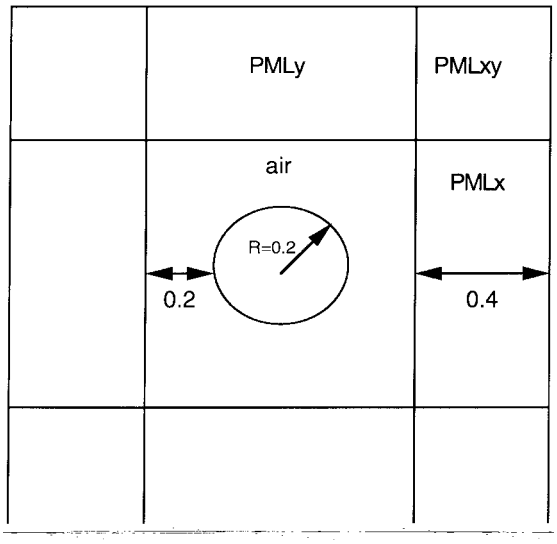

Fig. 6. Schematic of benchmark problem 3—the electric dipole.

$(a\phi_i,\ \phi_i,\ \phi_i)$ indicates that we use $a\phi_i$ as the basis function for the x component of $\vec{A}$ and ϕ_i as the basis function for y and z components of $\vec{A}$, respectively. It can be shown that under these sets of basis functions, all of the jump conditions are satisfied. For example, at point P in Fig. 1, vector potential $\vec{A}$ will have the following different values in the four different regions:

$$\begin{aligned} \text{interior domain}: &\quad (A_x,\ A_y,\ A_z) \\ \text{PML}x: &\quad (a_x A_x,\ A_y,\ A_z) \\ \text{PML}y: &\quad (A_x,\ a_y A_y,\ A_z) \\ \text{PML}xy: &\quad (a_x A_x,\ a_y A_y,\ A_z). \end{aligned} \tag{43a}$$

It is easy to see that these values satisfy (39)–(41).

In order to render a symmetric system, we keep the weighting functions the same as the basis functions and to simplify the implementation, we set $a_x = a_y = a_z = a$. After using $(a\phi_i,\ \phi_i,\ \phi_i)$ as the basis and weighting functions, $\vec{A}_{ij}$ in the PMLx material becomes as shown in (43b), at the bottom of the previous page. In contrast to the equivalent isotropic (i.e., interior region) matrix where off-diagonal terms vanish when at least one of node i and j is in a homogeneous subregion, in the PML, the off-diagonal terms are zero for all i and j (except at the outer boundary of the PML itself).

It is interesting to note that this numerical system is identical to the one that we would have obtained if we stretched the coordinate x using $x' = ax$, which is exactly the stretched coordinate approach to the PML. Hence, for our formulation, both the stretched coordinate and anisotropic medium implementations generate the exact same numerical system. They will certainly produce the same fields in nonPML regions. In the PML region, the fields may be interpreted differently for stretched coordinate and anisotropic media systems; however, interpretation of the fields in PML region does not have great significance since they are not part of the physical system.

IV. Benchmark Results

In this section, we present results from three sample benchmark problems which have been used to verify our formulations. The intent is to demonstrate that the computational underpinnings of the proposed PML approach lead to valid Maxwell equation solutions for nodal FEM's rather than to explore and optimize the parameter space associated with the PML itself (e.g., attenuation coefficient value/spatial distribution, layer thickness, etc.), which tends to be problem dependent. As a result, we have opted to maintain a constant coefficient PML region whose value can be estimated from normal incidence reflection coefficient analysis [2] and is well within the range considered by others (e.g., [6]). Further, the

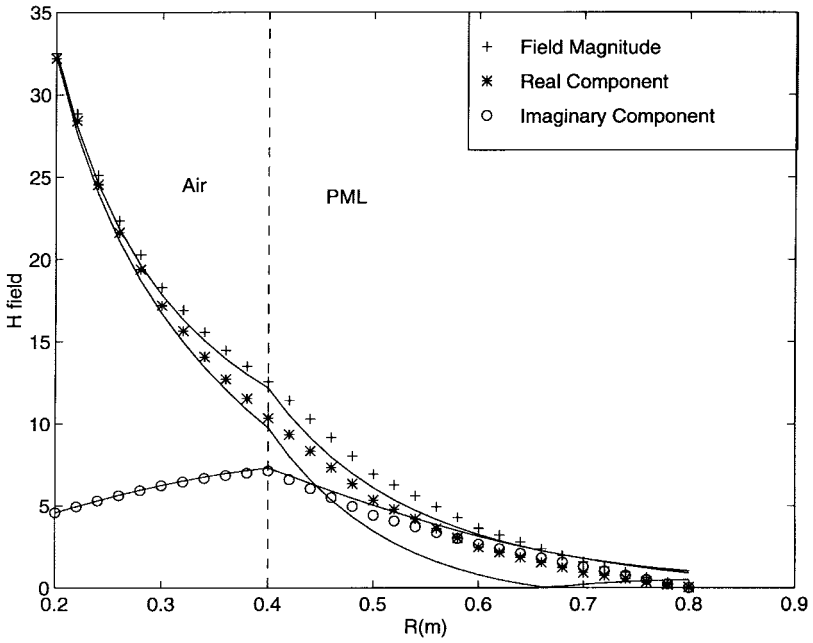

Fig. 7. Comparsion of the numerical (markers) and analytical (solidline) solution for benchmark problem 3.

layer thickness in terms of the numbers of elements, which span this distance, has been selected to be a representative average of those used by others [5], [6], [9]. It is also worth noting that while there have been reports of poor finite-element system matrix conditioning and concomitant poor iterative solver behavior associated with the PML when implemented for edge-element solution strategies [6], we have not observed any degradation in iterative solver performance in the examples presented herein. Clearly, our experience in this regard is anecdotal and more systematic study of this issue is warranted, although we have explored the PML parameter space in some depth in a specialty application and have not observed degraded iterative solver convergence when the PML was employed in a node-based finite-element scheme in this case either [15].

The first benchmark example involves the simulation of a plane wave normally incident on the PML as illustrated in Fig. 2. The interface between the interior domain and the PML occurs at $z = 0$. The H formulation (31) was used in this case on a tetrahrahedral finite-element mesh having dimensions of 0.4 × 0.4 × 1.0 m in the x, y, and z directions, respectively, with approximate sampling rates of 15 nodes/wavelength. The solution was driven at 200 Mhz by a unit-magnitude tangential magnetic field polarized in the $\hat{x}$ direction at $z = -0.5$ m. Boundary conditions at $y = \pm 0.2$ and $x = \pm 0.2$ were PEC (i.e., $\vec{n} \times \vec{E} = 0$) and PMC (i.e., $\vec{n} \times \vec{H} = 0$), respectively. The PML, itself, was terminated with PEC conditions and utilized complex number $a = 1 - 2i$ as its attenuation factor. The analytical solution for this example is quite simple:

$$\vec{H} = \begin{matrix} \vec{H}_o e^{-jkz} & z < 0 \\ \vec{H}_o e^{-jkz} e^{-k\beta z} & z > 0. \end{matrix} \tag{44}$$

Fig. 3 provides a comparison of the numerical and analytical results for the $\vec{H}$ field in this case. The solid lines indicate the exact solutions whereas the markers depict the computed real, imaginary, and magnitude components. As can be seen, the agreement is excellent with the maximum error in any of the numerical curvers in Fig. 3 being less than 1.2%. Similar calculations and results (not shown) have been obtained with the $A - \Phi$ formulation under Lorentz gauge #2 with nearly identical computational precision.

The second more challenging benchmark problem is that of an infinite cylindrical radiator in free-space. Fig. 4 illustrates a cross section of the computational domain and indicates the relevant geometrical dimensions that have been used. In this case, a unit-magnitude tangential electric field polarized in the azimuthal direction oscillating at a 200-Mhz excitation frequency has been imposed on the cylinder surface. The analytical solution to this problem is

$$\vec{E} = \frac{H_1^1(kr)}{H_1^1(kR)} \hat{\phi} \tag{45}$$

which is one-dimensional, but the computations have been carried out on a fully 3-D mesh (with similar sampling rates as in the first benchmark) and the results have been compared along the midplane of the computational domain. The cylinder was 1.6 m tall with PMC conditions imposed on its top and bottom surfaces. As indicated in Fig. 4, the PML was Cartesian in geometry, consisted of six layers, used $a = 1 - 2i$ as its attenuation factor, and was terminated by PEC conditions similar to those used in the previous example.

Comparison of the computed and analytical results are shown in Fig. 5. Again the agreement is excellent with maximum errors being less 1% for the magnitude and the real part of the E field and no worse than 5% for the imaginary part of the solution. The numerical results in this figure were generated with the $A-\Phi$ approach. Using the H formulation to compute the corresponding dual problem generates an almost identical numerical solution (the maximum difference between the two numerical computations was less than 0.01%).

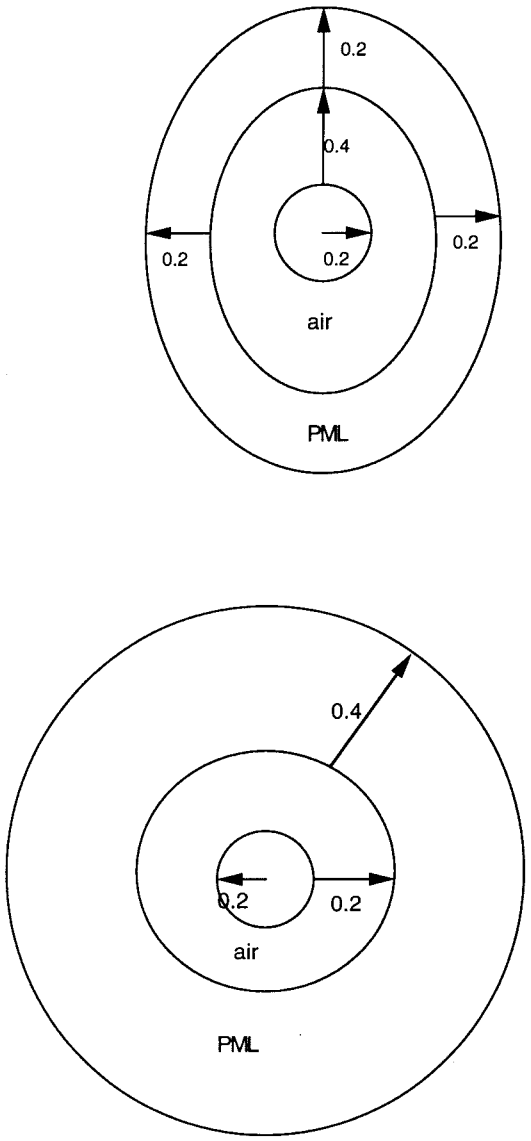

Fig. 8. Geometry of two benchmark problems for the arbitrarily shaped PML algorithm.

The third and final benchmark to be reported here is the electric dipole problem. As a computational simulation of this solution, we constructed a 3-D mesh of a hollow sphere embedded inside a Cartesian rectangular box surrounded by PML's as indicated in Fig. 6. For a short electric dipole, the H field has only a $\hat{\phi}$ component

$$H_\phi = e^{-jkr}\left(\frac{jk}{r} + \frac{1}{r^2}\right)\sin(\theta) \tag{46}$$

which we used to specify the tangential component of $\vec{H}$ on the spherical surface in order to drive our computational solution. The PML characteristics were the same as those in the previous two examples. Fig. 7 shows a comparison between numerical and analytical calculations. Results are again very favorable with maximum errors being less than 2.4% for either the H or $A - \Phi$ calculations.

V. Arbitrarily Shaped PML

The requirement of a Cartesian mesh termination imposed by the usual PML treatment is somewhat cumbersome for finite elements and serves to constrain the flexibility of the method in terms of representing complex shapes. Three-dimensional mesh generation is already difficult enough without the additional insistence on a Cartesian termination with predefined specifications for corner, edge, and face regions. In this section, we provide and test an approach for extending the conventional Cartesian PML formulation to one that can be adapted to a more arbitrary shape. The key in realizing this approach is to recognize that in our formulations the anisotropic and stretched coordinate frameworks lead to identical discrete systems, as illustrated in Section III. In the arbitrarily shaped PML context, it is much more natural to adopt the stretched coordinate view. Specifically, instead of modifying the finite-element equations based on material property changes with predefined layer regions in order to eliminate all reflections, we stretch the finite-element mesh coordinates within the PML by enacting the complex coordinate transformation while leaving the finite-element equations themselves essentially unaltered. By adopting this approach we can virtually have an unlimited number of PML regions which are defined by nodal-mesh coordinates that can be deployed to form a more arbitrary shape. Our scheme proceeds as follows.

1) Generate the 3-D mesh with a suitable convex layer such that the interface between this layer and the interior domain will be a closed convex surface.
2) For each FEM node at position $\vec{x}$ within the PML, find the point on the outer surface of the interior domain that is closest to $\vec{x}$ and designate it as $\vec{x}_o$.
3) Construct a new coordinate for each $\vec{x}$ as $\vec{x}_{\text{new}} = \vec{x}_o + a(\vec{x} - \vec{x}_o)$ where a is the same complex number used to characterize the media in the anisotropic PML approach.

In essence, this algorithm stretches the nodal coordinate in the PML region along the direction normal to the outer surface of the interior domain. It provides the identical discrete system to that obtained with the Cartesian anisotropic media mesh termination when the arbitrary surrounding PML is a rectangular box.

Here, we present two test cases for this non-Cartesian PML algorithm using the cylindrical radiator test case of Fig. 4 but with cylindrical and ellipsoidal terminations. The respective geometries for these problems are illustrated in Fig. 8. The numerical computations (compared to their analytical counterparts) for these non-Cartesian PML terminations are shown in Fig. 9. While we have not exhaustively tested this approach, the results are very encouraging. The errors introduced by the presence of the PML are comparable to those for the Cartesian terminations shown in Fig. 5 and can be achieved with any of the formulations described in Section II.

VI. Conclusions

A node-based implementation of the PML concept for finite-element frequency-domain electromagnetic scattering has been presented. The development is set in the context of the

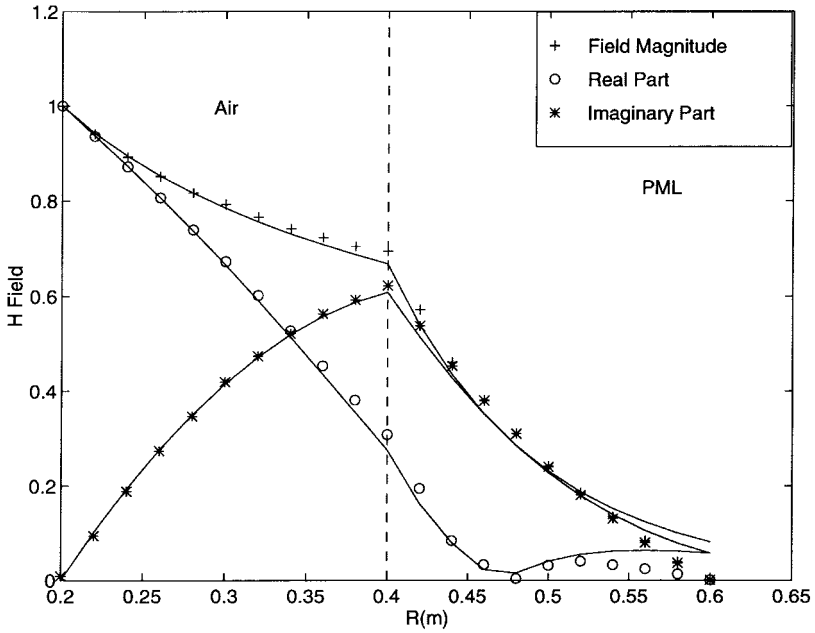

Fig. 9. Comparison of the numerical (markers) and analytical (solid line) solution for the cylindrical radiator with a cylindrical PML layer.

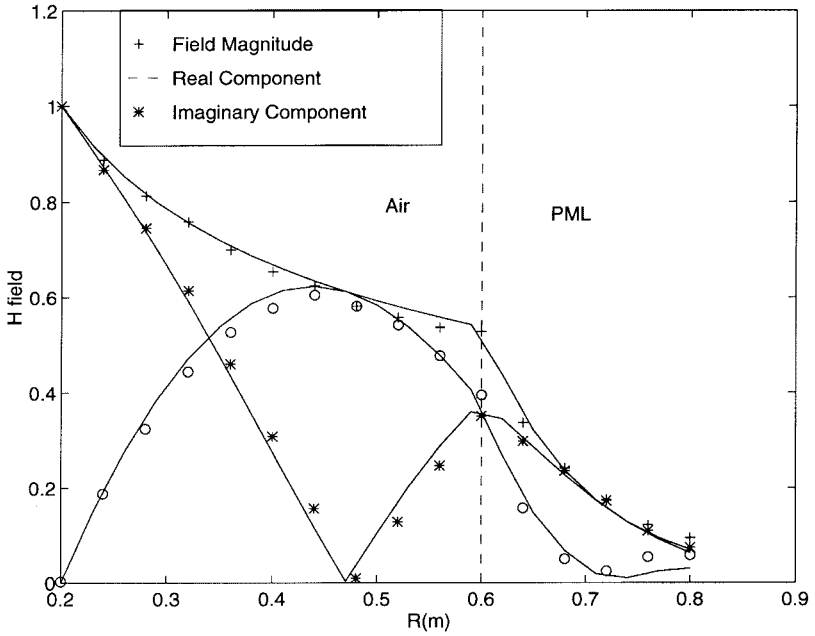

Fig. 10. Comparison of the numerical (markers) and analytical (solid line) solution of the cylindrical radiator with an elliptical PML layer.

generalized scalar/vector potential formulations of Boyse *et al.* [11]. In doing so, determination of the appropriate gauge condition for the PML region is required and the analogous gauge conditions for both coupled and decoupled (i.e., direct field) systems have been determined. Use of a material dependent basis/weighting function produces a symmetric discrete system, which is identical (in all components) from either the anisotropic or stretched coordinate viewpoints of the PML mesh termination. This equivalency leads to a simple approach for realizing non-Cartesian mesh terminations, which are more natural for finite-element discretizations in the sense that they can be arbitrarily shaped which has been a hallmark of the success of finite elements. Benchmark results for three example problems using both Cartesian/non-Cartesian mesh terminations and $A - \Phi$, E, and H formulations have been shown with promising results.

REFERENCES

[1] J. P. Berenger, "A perfectly matched layer for the absorption of electromagnetic waves," *J. Comput. Phys.*, vol. 114, pp. 185–200, Oct. 1994.

[2] Z. S. Sacks, D. M. Kingsland, R. Lee, and J. F. Lee, "A perfectly matched anisotropic absorber for use as an absorbing boundary condition," *IEEE Trans. Antennas Propagat.*, vol. 43, pp. 1460–1463, Dec. 1995.

[3] C. M. Rappaport, "Perfectly matched absorbing boundary conditions based on anisotropic lossy mapping of space," *IEEE Microwave Guided Wave Lett.*, vol. 5, pp. 90–92, Mar. 1995.
[4] W. C. Chew and W. H. Weedon, "A 3-D perfectly matched medium from modified Maxwell's equations with stretched coordinates," *Microwave Opt. Technol. Lett.*, vol. 7, pp. 599–604, Sept. 1994.
[5] L. Zhao and A. C. Cangellaris, "GT-PML: Generalized theory of perfectly matched layers and its application to the reflectionless truncation of finite-difference time-domain grids," *IEEE Trans. Microwave Theory Technol.*, vol. 44, pp. 2555–2563, Dec. 1996.
[6] J. Y. Wu, D. M. Kingsland, J. F. Lee, and R. Lee, "A comparison of anisotropic PML to Berenger's PML and its application to the finite-element method for EM scattering," *IEEE Trans. Antennas Propagat.*, vol. 45, pp. 40–50, Jan. 1997.
[7] R. Mittra and U. Pekel, "A new look at the perfectly matched layer (PML) concept for the reflectionless absorption of electromagnetic waves," *IEEE Microwave Guided Wave Lett.*, vol. 5, pp. 84–86, Mar. 1995.
[8] D. Katz, E. Thiele, and A. Taflove, "Validation and extension to three dimensions of the Berenger PML absorbing boundary condition," *IEEE Microwave Guided Wave Lett.*, vol. 4, pp. 268–270, Aug. 1994.
[9] L. Zhao and A. C. Cangellaris, "A general approach for the development of unsplit-field time domain implementations of perfectly matched layers for FDTD grid truncation," *IEEE Microwave Guided Wave Lett.*, vol. 6, pp. 209–211, May 1996.
[10] J. C. Veihl and R. Mittra, "An efficient implementation of Berenger's perfectly matched layer (PML) for finite difference time domain mesh truncation," *IEEE Microwave Guided Wave Lett.*, vol. 6, pp. 94–96, Feb. 1996.
[11] W. E. Boyse, D. R. Lynch, K. D. Paulsen, and G. N. Minerbo, "Nodal-based finite-element modeling of Maxwell's equations in three dimensions," *IEEE Trans. Antennas Propagat.*, vol. 40, pp. 642–651, June 1992.
[12] W. E. Boyse and K. D. Paulsen, "Accurate solutions of Maxwell's equations around PEC corners and highly curved surfaces using nodal finite elements," *IEEE Trans. Antennas Propagat.*, vol. 45, pp. 1758–1767, Dec. 1997.
[13] K. D. Paulsen, W. E. Boyse, and D. R. Lynch, "Continuous potential Maxwell solutions on nodal-based finite elements," *IEEE Trans. Antennas Propagat.*, vol. 40, pp. 1192–1200, Oct. 1992.
[14] K. D. Paulsen and D. R. Lynch, "Elimination of vector parasites in finite element Maxwell solutions," *IEEE Trans. Microwave Theory Tech.*, vol. 39, pp. 395–404, Mar. 1991.
[15] J. Tang and K. D. Paulsen, "Evaluation of perfectly matched layer mesh terminations in finite element bioelectromagnetic scattering computations," *IEEE Trans Biomed. Eng.*, to be published.

Jingwu Tang received the B.S. degree in mechanical engineering from Peking University, China, in 1991, and the M.S. degree in electrical engineering from the Thayer School of Engineering, Dartmouth College, Hanover, NH, in 1997.

He is currently employed at OneWave Inc., Watertown, MA, as a Software Engineer. His research interest is the application of finite-element methods in computational electromagnetics.

Keith D. Paulsen received the B.S. degree in biomedical engineering from Duke University, Durham, NC, in 1981, and the M.S. and Ph.D. degrees in biomedical engineering from Dartmouth College, Hanover, NH, in 1984 and 1986, respectively.

From 1986 to 1988, he was an Assistant Professor in the Electromagnetics Group within the Department of Electrical and Computer Engineering, University of Arizona, Tucson. He is currently an Associate Professor at the Thayer School of Engineering, Dartmouth College and the Director of the Radiobiology and Bioengineering Research Program for the Norris Cotton Cancer Center within the Dartmouth–Hitchcock Medical Center, Lebanon, NH. His research interests include numerical electromagnetics, with particular emphasis on biomedical problems in cancer therapy and imaging.

Shah A. Haider received the B.Sc.Eng. (electrical and electronics) degree from the Bangladesh University of Engineering and Technology, Dhaka, Bangladesh, in 1977, and the M.S. and Ph.D. degrees in electrical engineering from the University of Arizona, Tucson, in 1988 and 1996, respectively.

From 1978 to 1985, prior to joining the University of Arizona, Tucson, he worked as an Assistant Engineer in Bangladesh Power Development Board, an Electrical Engineer at the Ministry of Electricity, Libya, and an Electrical Engineer at the National Petrochemical Company, Marsa Al-Brega, Libya. From 1986 to 1995, during his graduate studies, he was a Research Associate in the Radiation Oncology Department at the University of Arizona. Currently, he is a Postdoctoral Research Associate at the Thayer School of Engineering, Dartmouth College, Hanover, NH. His current interests include numerical methods in electromagnetics (especially finite-element methods) and its application to biomedical engineering, microwave engineering, and integrated circuit technology.

Dr. Haider was awarded the First Prize in the 9th All Pakistan National Fair (1970) and received the National Science and Technological Fellowship (1977–1978) to work at the Bangladesh Council of Scientific and Industrial Research Laboratories, Dhaka. He was the recipient of the Curtis Carl Johnson Memorial Award of Bioelectromagnetics Society (BEMS) for the Best Student Paper presented in its 11th Annual Meeting (1989). He is a member of Eta Kappa Nu.